Human Mars Entry, Descent and Landing Architecture Study: Deployable Decelerators

Alicia Dwyer Cianciolo[1], Robert Dillman[2], Andrew Brune[3], Rafael Lugo[4]
NASA Langley Research Center, Hampton, VA, 23681, U.S.A.

Tara P. Polsgrove[5], Thomas K. Percy[6], Steve Sutherlin[7]
NASA Marshall Space Flight Center, Huntsville, AL, 35812, U.S.A.

and
Alan Cassell[8]
NASA Ames Research Center, Moffett Field, CA, 94035-1000, U.S.A.

NASA's Entry, Descent and Landing Architecture Study uses a trajectory simulation framework to evaluate various technologies and concepts of operations for human scale EDL at Mars. The study results inform agency technology investments. This paper summarizes the design assumptions and analysis of two deployable entry concepts performed in Phase 2 of the study. The entry concepts include a rigid deployable called the Adaptable Deployable Entry Placement Technology and an inflatable concept called the Hypersonic Inflatable Aerodynamic Decelerator. This paper describes the concept operations of these vehicles to deliver a 20-metric ton payload to the surface of Mars. Details of vehicle design and flight performance are summarized along with results of analysis on the aft body heating and its effect on the payload. Finally, recommended technology investments based on the results are presented.

I. Introduction

Several technology investments are required to develop Mars human scale Entry, Descent, and Landing (EDL) systems. In a resource-constrained environment, studies play the critical role of identifying the most feasible technical path and high payoff investments. One such NASA multi-directorate, multi-center study, is called the Entry, Descent and Landing Architecture Study (EDLAS). Phase 1 of the EDLAS, performed in 2016, developed point designs for four unique entry technologies to deliver a specified 20 t human scale payload to the Mars surface. Summaries of the Phase 1 designs are provided in references [1-3]. The objective of EDLAS Phase 2, performed in 2017, was to advance each concept to a level that enabled fair comparison of respective design strengths and weaknesses. Additionally, Phase 2 analysis considered vehicle design updates for descent and landing based on improved understanding of vehicle integration and flight performance. This paper summarizes the analysis performed to update the two revolutionary deployable concepts, a rigid deployable, called the Adaptable Deployable Entry Placement Technology (ADEPT) and an inflatable deployable called the Hypersonic Inflatable Aerodynamic Decelerator (HIAD). Images of each vehicle, without a payload, are shown in Figure 1. Details of the other vehicle configurations considered in the EDLAS Phase 2 study are found in references [4].

NASA's Human Exploration and Operations Mission Directorate (HEOMD) provides ground rules and assumptions for the Mars architecture and Mars surface lander payload manifests used in this study. Each decelerator is integrated

[1] Aerospace Engineer, Atmospheric Flight and Entry Systems Branch (AFESB), AIAA Senior Member.
[2] Aerospace Engineer, AFESB, AIAA Senior Member.
[3] Aerospace Engineer, Structural and Thermal Branch, Engineering Directorate, Member AIAA.
[4] Aerospace Engineer, Analytical Mechanics Associates, AFESB, Engineering Directorate AIAA Member.
[5] Aerospace Engineer, Exploration System Development Branch.
[6] Aerospace Engineer, MSFC Advanced Concepts Office, AIAA Member.
[7] Aerospace Technologist, Propulsion Systems and Technologies, Advanced Concepts Office.
[8] Aerospace Engineer, Entry Systems and Vehicle Development Branch.

with the four HEOMD defined payload configurations. While the description of the architecture and assumptions is provided elsewhere [5], Section II presents the concept of operations for each deployable vehicle, identifies common subsystems and establishes mass sizing and margin policies that are integrated into the Master Equipment List (MEL).

The deployable vehicles use a 70 deg sphere cone forebody shape similar to previous Mars landers. The deployable diameters are designed to also maintain heritage Mars entry vehicle ballistic coefficients and similar low lift-to-drag (L/D) ratios. In contrast to robotic missions to the planet, the human scale concept of operations does not jettison ballast mass nor separate a backshell or a heatshield prior to landing. The difference is due to the fact that multiple landers are delivered to the same surface location. Eliminating jettison events reduces risk of impacting critical pre-deployed surface assets. Additionally, human scale missions will not use parachutes as a primary drag device. Parachutes do not scale well for these large entry vehicles. The large mass increase requires a parachute drag area that is not achievable in a single chute or even clusters. Likewise, large vehicle diameter increases the parachute trailing distance to 100's of meters making chutes infeasible. Therefore, engines are used to slow the vehicles for descent and landing and must initiate while the vehicle is still traveling at supersonic speeds. The study assumes that all thrust variations are performed using differential throttling, not gimbaled engines. Eight 100 kN engines throttled at 80% is the nominal thrust level (640 kN) to accommodate dispersions.

(a) ADEPT (b) HIAD

Figure 1. Images of the EDLAS Deployable Decelerator concepts.

The current deployable vehicle designs do not include a backshell. While this allows for lower vehicle gross masses, it does increase the risk of damage to the payload from micro meteor and orbit debris (MMOD), environmental heating during aerocapture and entry, and from surface debris on approach and landing. This study addresses the environmental concerns by characterizing the heating on the aftbody using two different approaches. The first approach addresses the problem from the flight mechanics perspective that considered options to minimize the angle of attack. The second approach used Computational Fluid Dynamics (CFD) to analyze the heating on the aft body for the reduced angles of attack. The results of the two approaches are key to understanding the thermal protection mass required to mitigating heating on payload, to determine if local thermal protection systems (TPS) on individual payload elements is sufficient or if a more substantial and massive backshell structure is needed. Sections III and IV summarize flight performance and payload protection analysis, used to support the aftbody mass assessment.

A primary objective of EDLAS is to provide the NASA Space Technology Mission Directorate (STMD) with investment recommendations. Therefore, Section V presents the study recommendations based on the low L/D analysis presented herein.

II. Vehicle Design and Concept of Operations

A key objective of the architecture study is to ensure that the vehicle design is compatible with all phases of the mission. EDLAS considers Earth launch through surface operations at Mars. Past studies have considered Earth prelaunch facility accommodations [6] so they are not included. Likewise, a description of the Mars architecture used for this study is provided in Ref [5] and is not repeated here. It is noted that the study assumes that four (three cargo and one crew) landers are required to support a 300-day mission. While the payload configurations are different, the EDL sequence is identical for each lander using a specific entry technology. This consistent sequence enables the cargo landers to serve as end-to-end flight demonstrations for the fourth crew entry vehicle. The following subsections describe the vehicle configurations in each phase of flight for the ADEPT and HIAD. Additionally, the detailed EDL concept of operations is provided. While the configurations and concepts of operations for the ADEPT and HIAD are similar, key differences are noted.

A. ADEPT

A detailed description of the ADEPT vehicle is provided in [2]. EDLAS Phase 2 updates to the configuration, including a revised mass model and a description of the concept of operations, are presented here. Figure 2 depicts a bottom and side view of the ADEPT vehicle with dimensions. The ribs on one side are longer than those on the other

creating a forebody with an asymmetric shape to achieve the desired lift-to-drag ratio and the same deployable system is used for both aerocapture and EDL.

The revised mass model identifies subsystems common to all the EDL vehicles being considered (e.g. avionics, power, and thermal management) and applied common margin policies across vehicle subsystems including structures, thermal protection system and propulsion. The primary ADEPT components include (1) the rigid nose, (2) the deployable decelerator, (3) ribs and struts, and (4) the deployment system and integration with the lander structure. A description of each, along with the mass estimate is provided. The rigid nose mass estimate of 2640 kg is based on heritage SLA561V TPS [7], a composite carrier structure that includes compression pads and upper stage adapter, as well as a seal between rigid nose and the deployable carbon fabric. The structure also includes engine nozzle and landing leg exit doors. Since no elements can be jettisoned, it is assumed that the doors slide open during entry after peak dynamic pressure. The structure mass for this element includes 40% Mass Growth Allowance (MGA) and the rigid heatshield TPS is sized using a 30% MGA. The deployable decelerator mass estimate was 1199 kg. Its thickness and mass are based on TPS performance in ground testing and includes carbon fabric acreage, rib shielding and insulation layers, as well as aft side contamination and thermal blanket for payload (leveraging HIAD sizing). The deployable decelerator mass includes 30% MGA. The ribs and struts mass estimate was 1427 kg, which is based on engineering fidelity Finite Element model (Calculix [8]). It also assumes that the ribs are made of Graphite composite material with titanium struts. The mass estimate includes fittings, fasteners, and thermal protection for struts and includes 30% MGA. Finally, the deployable system mass estimate was 1347 kg. This estimate is based on the 2 m Ground Test Article [9] and includes a movable ring, structural interface to lander stage, joints, instrumentation, motors and actuators, feedback control, thermal protection and includes a 30% MGA. The Master Equipment for ADEPT, including current best estimate (CBE) and maximum estimated value (MEV), is provided in Table 1. Therefore, the total MEV mass for the ADEPT aeroshell was nearly 8.7t.

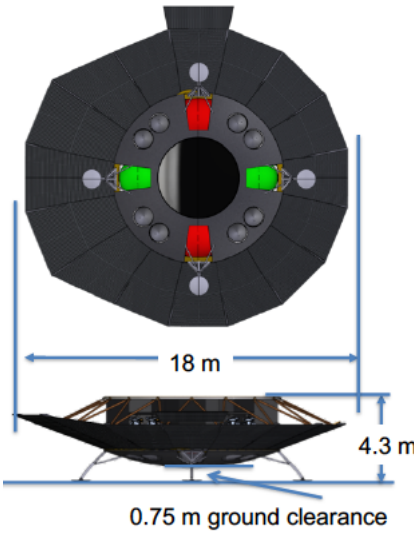

Figure 2. ADEPT bottom and side images with dimensions.

Table 1. ADEPT Aeroshell Master Equipment List.

Element	CBE (kg)	MGA %	MGA (kg)	MEV (kg)
Rigid Nose	**1892**	**40**	**748**	**2640**
TPS	294	30	88	382
Carrier Structure	698	30	210	908
Compression Pads/LV Adapter Interface	300	50	150	450
Seal/Rigid Nose Transition to fabric decelerator	100	50	50	150
MDM Nozzle Exit Access	250	50	125	375
Landing Gear Access	250	50	125	375
Deployable Decelerator	**1790**	**38**	**687**	**2477**
3d Woven TPS- Carbon Fabric Acreage	922	30	277	1199
3d Woven Fabric TPS Joints	68	30	20	88
Stitching Treatments	50	30	15	65
Launch Restraint System	200	50	100	300
Rope Stiffeners- Rib to Rib	150	50	75	225
Aft Side contamination & Thermal Blanket	400	50	200	600
Ribs & Struts	**1090**	**30**	**337**	**1427**
Ribs	400	30	120	520
Struts	390	30	117	507
End Fittings	250	30	75	325
Thermal Protection	50	50	25	75

Trim Tabs	***590***	***30***	***177***	***767***
Forward Ring	*590*	*30*	*177*	*767*
Deployment System & DM Integration	**1036**	**30**	**311**	**1347**
Deployment System	700	30	210	910
Structural Interface to Descent Module	200	30	60	260
Joints/Fasteners/etc.	86	30	26	112
Thermal	50	30	15	65
TOTALS	**6398**	**35**	**2260**	**8658**

Figure 3 shows the ADEPT vehicle configuration in each phase of the mission. In the *Launch* configuration, the rigid deployable is folded forward of the rigid heatshield, toward the lower portion of the SLS 10 m fairing so that it does not impact the packaging volume for the payload. A detailed image of ADEPT in the stowed configuration is provided in Figure 4a. After launch, the ADEPT vehicle deploys the decelerator in Earth orbit for check out prior to transit to Mars. The *Transit* configuration in Figure 3 shows the ADEPT lander docked with the in-space transportation stage. The image depicts adequate clearance between the solar arrays of the transportation stage and the ADEPT lander. Once at Mars, the cargo missions perform aerocapture into a one Sol orbit (250 km x 33800 km). Therefore, two days prior to Mars arrival, the lander separates from the transportation stage and reorients for aerocapture. The asymmetric lander uses three flaps for flight control in the atmosphere during the aerocapture and EDL. A flap is notionally shown in the Figure 3 *Mars Arrival* configuration. An image with all three flaps is provided in Figure 4b (each one extends beyond the outer diameter of the aeroshell) and a discussion of the flight control approach is provided in the next section. During transit, the lander is powered by the transportation stage. After separation and aerocapture, the lander must generate its own power in orbit for up to one year. Therefore, the *Mars Orbit* configuration shows solar arrays deployed. Radiators, required for thermal management of the payload and main engine propellants, are mounted around the base of the lander and remain exposed to the space environment throughout the mission. For the lander that will deliver crew to the surface, it must dock with the crew transfer vehicle in a configuration that is opposite from the cargo lander during transit (connected through the heat shield) so crew can enter directly into the habitat. The *Crew Transfer* image in Figure 3 shows that there is appropriate clearance from the transit stage solar arrays assuming the orbiting arrays on the crew lander are stowed or jettisoned prior to docking.

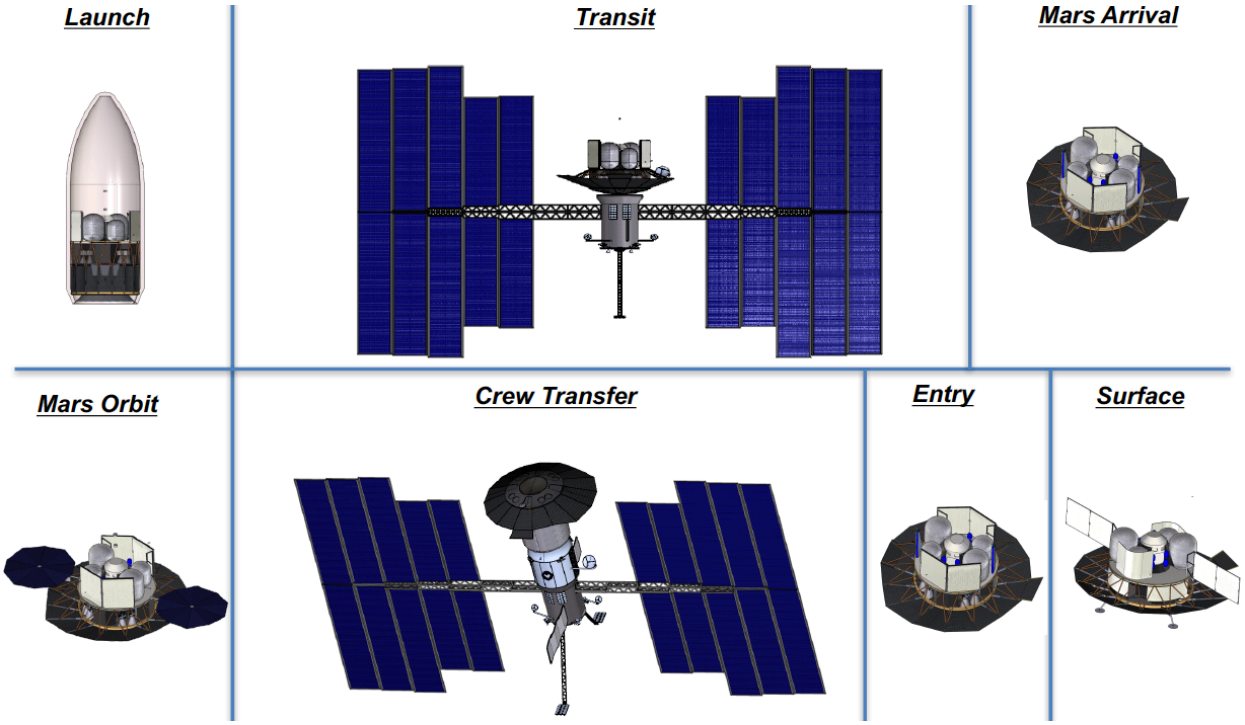

Figure 3. ADEPT vehicle configurations for each phase of the mission.

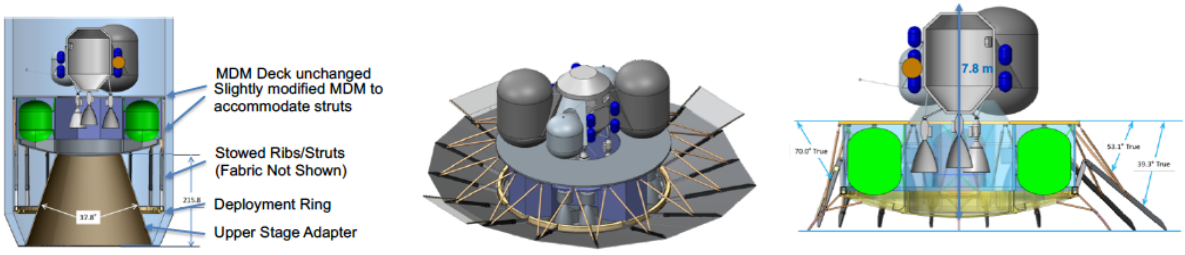

(a) (b) (c)

Figure 4. Additional details illustrated for ADEPT (a) launch configuration, (b) aerocapture and entry configuration with three flaps and (c) landed configuration to allow for cargo access.

As mentioned above, three cargo landers are delivered to Mars, perform aerocapture and final checkout in orbit prior to initiating deorbit and EDL. After checkout and proper phasing is achieved, the cargo landers jettison the solar arrays depicted in the *Mars Orbit* image, perform the deorbit burn and reorient for entry. Since control approach is the same for aerocapture and entry, the vehicle configurations for *Mars Arrival* and *Entry* are identical as shown in Figure 3. One key difference from earlier human scale EDL studies [10-12] is that no elements are being jettisoned during EDL. To minimize cargo needed, the current Mars architecture sends all landers to the same landing zone. The landers are required to land within 50 m of a designated target and no closer than 1 km from any previously landed assets to reduce the risk of impact from the descent engines uplifting regolith. Once on the surface, radiators are deployed to provide thermal management of the cryogenic storage facility in the MAV cargo lander. The landers are equipped with batteries that are sized to support operations on the surface for one Sol to allow time to connect to the previously landed surface power supply. The vehicle is shown in the *Surface* configuration image in Figure 3. Again, a more detailed image of a notional surface retraction concept is provided in Figure 4c. Many events occur during EDL, therefore Figure 4 shows the details of the sequence for the ADEPT vehicle. The vehicle enters with the deployed rigid heatshield. At approximately Mach 3, the vehicle attitude is changed to zero degrees angle of attack and initiates engines for descent and touchdown.

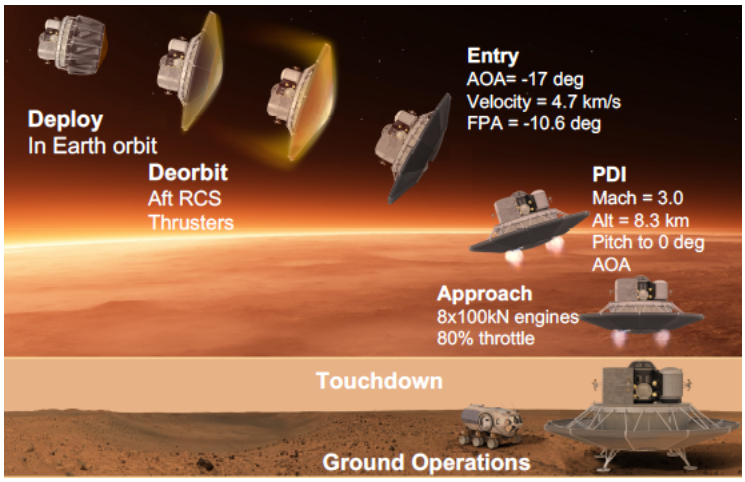

Figure 5. ADEPT vehicle EDL concept of operations.

B. HIAD

Unlike the ADEPT heat shield that has been shown to tolerate the combined aerocapture and entry heat pulses, the flexible TPS that covers the inflatable structure of the HIAD has not yet been tested against a dual heat pulse. Therefore, for this study, the decision was made to include two complete HIAD systems (including the 9.1 m diameter rigid heatshield), despite the added mass. Using a second HIAD ensured pristine TPS for EDL, and jettisoning the first aeroshell just after the aerocapture pass reduced the overall mass of the EDL vehicle. To maintain the same ballistic coefficient (~150 kg/m^2) for both aeropasses, the entry HIAD diameter was slightly smaller, at 16.4 m, than the 17.2 m aerocapture HIAD. Figure 6 shows an image of the HIAD EDL vehicle bottom view with engine and landing gear, and a side view showing the nominal ground clearance and lander deck height. It is noted that the aerocapture rigid heatshield center body does not need doors for the engines or landing gear, since the main engines are not used. Future concepts are considering ways to attach two HIAD inflatable structures to the same center rigid heatshield to save additional mass. Details of the current HIAD design are provided in Ref [3]; only updates to the point design mass model are presented here.

The HIAD mass model is based on a manufactured 6 m diameter test article, therefore the design was allowed to use a smaller MGA for some components than the ADEPT vehicle. The five primary components and their

subcomponents, listed in Table 2, include (1) the rigid nose heatshield, (2) inflatable structure, (3) the inflation system, (4) thermal protection and (5) aerocapture HIAD separation system. A description of the component masses and sizing rational are provided below.

The first major component is the center rigid heatshield, which is similar to the one used on ADEPT, with modifications to accommodate the inflatable structures as well as attaching the second aeroshell. The rigid heatshield structural mass estimate is based on the HIAD team's NASTRAN model with 20% MGA, and since the aerocapture rigid nose does not need doors for the main engines and landing gear it is lighter than the EDL rigid nose. The HIAD rigid noses are also lighter than the ADEPT rigid nose, both because the HIAD TPS is lighter than ADEPT's and also because the inflatable structure transfers the load into the rigid center in a more distributed fashion than the individual structural ribs used on ADEPT.

Additional subcomponents of the rigid nose include the HIAD attachment ring and adapter mass. The adapter mass is a placeholder for structure that will interface with the lander structure and the launch vehicle adapter. These are currently not well enough defined for a detailed mass estimate, but the mass will be similar to ADEPT's structural adapter (590kg x1.3 = 767kg).

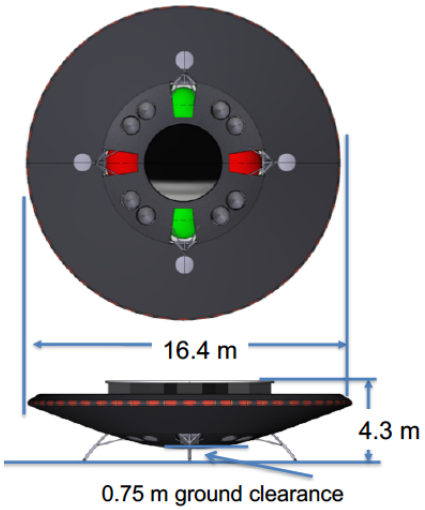

Figure 6. HIAD bottom and side images.

An inflatable alternative to mechanical doors in the EDL rigid nose was also investigated, as shown in Figure 7. This "Gap Filler" concept used smaller tori under HIAD's flexible TPS to fill the space where doors would be needed. After peak heating and prior to engine initiation, the tori would be deflated and retracted to expose landing gear and engines. These are presented to show illustrate the range of design options, but are not included in the total mass since rigid doors are already listed.

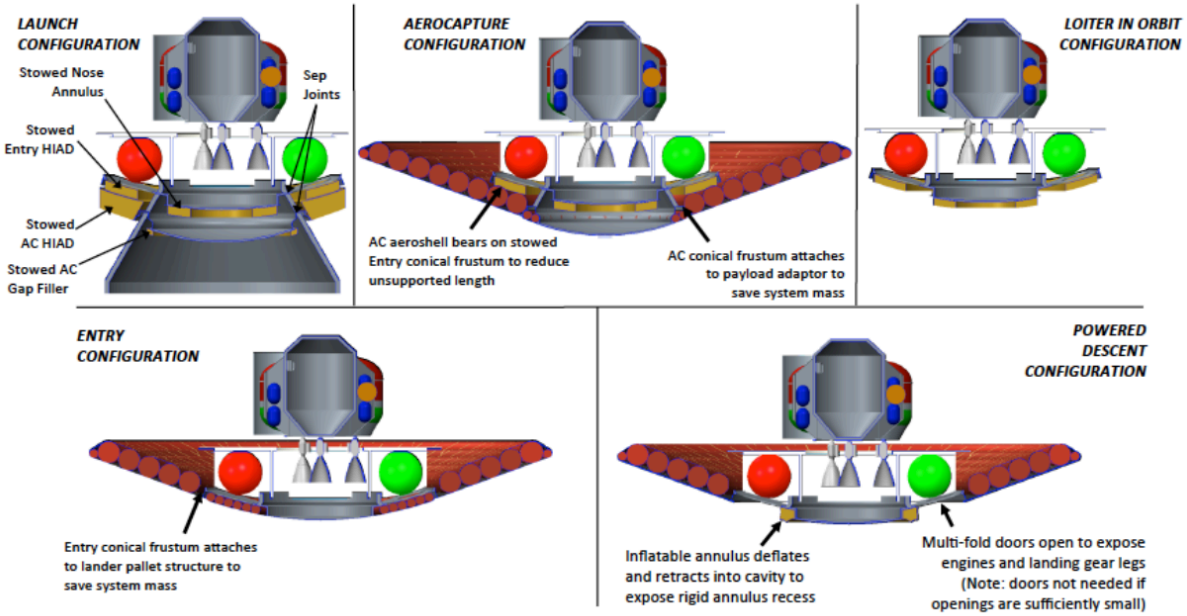

Figure 7. HIAD stowed and deployed configurations.

The second major component is the inflatable structure. Its estimated mass was generated using a HIAD tool developed from component and assembly masses of a 6m HIAD, individually measured during fabrication. The mass includes the torus liner, liner overlap, braid, braid overlap, coatings and adhesives, interference bonds, structural webbing, buffer panels, pairing loops, inflation and sense lines, and pressure ports. To simplify fabrication, the mass estimate assumes all tori use the same minor diameter of 0.70 m, and uses 7 tori of varying circumference to create the larger diameter aerocapture structure, and 6 tori to produce the EDL structure. The mass estimate was correlated to the Inflatable Reentry Vehicles Experiment (IRVE-3) 3m flight unit and 3.7m test articles [13].

The third major component is the inflation system. Two separate inflation systems are used, one for each HIAD. The aerocapture HIAD sees approximately half the dynamic pressure of the EDL system in flight, so the aerocapture HIAD operates at a lower pressure and has a lower inflation system mass. The inflation system mass estimate is based on the IRVE-3 flight system [13] and includes valves, check valves, inflation manifolds, pressure relief ports, mounting brackets, tubing, adapter fittings, ground servicing connections, and safety lockouts. The system for Mars use differs from the design used on the IRVE flights in that it replaces the dry nitrogen bottles used on the IRVE sounding rocket missions with nitrogen gas generators more appropriate for interplanetary flight. The mass model carries 20% MGA for the inflation system and a 25% MGA on the mass of the gas generators, which are larger versions of the current commercially available nitrogen generators, repackaged for flight use.

The inflatable tori are covered with a non-ablative flexible TPS that protects the vehicle during aerocapture and entry. The large vehicle diameter and relatively lower entry speeds (6.2 km/s for aerocapture and 4.5 km/s for Entry from the 1 Sol orbit) translate into lower heating loads than traditional capsule configurations. The heating can be mitigated using a lightweight flexible material. The material thickness and mass are based on TPS performance in HIAD ground testing. The mass estimate includes an outer fabric, insulation layers, gas barrier, seaming, and quilting. Trajectory and CFD analysis provide estimates of both convective and radiative heating. Due to uncertainty in the heating estimates, a factor of 1.4 is applied to the convective heat flux and a factor of 1.5 is applied to the radiative flux. Likewise, a factor of 1.3 is applied to the total heat load. Additionally, a 10% MGA is included for each. Therefore, the total margin for convective and radiative heating is shown in equations 1 and 2.

$$1.4*1.3*1.1 = \text{x2.0 factor on convective} \tag{1}$$

$$1.5*1.3*1.1 = \text{x2.1 factor on radiative} \tag{2}$$

Additional mass estimates are provided for the aerocapture HIAD separation system and retraction system. Like the heritage Mars heatshield separation systems, the HIAD separation system uses pyrotechnic fasteners to hold the HIAD in place for launch and flight to Mars, and releases the aerocapture HIAD on command. The aerocapture HIAD will be released before orbit circularization at the end of the aeropass. The separation system (215kg on aerocapture HIAD, 28kg on EDL structure) carries 100% MGA due to uncertainty in design requirements. Once the vehicle lands on the surface of Mars the EDL HIAD pressure is vented while motors on the perimeter of the lander pull Kevlar cords to retract the HIAD back into the side of the lander to simplify cargo offloading. The mass estimate for the retraction system is 150 kg with 33% MGA.

The final HIAD system mass element included in the MEL is the estimate for the flaps (291kg AC, 316kg EDL). Unlike the straightforward approach of attaching the tabs to the rigid outer diameter of the ADEPT structure, no final decision has been made as to how the HIAD vehicle will produce adequate flight control to meet the constrained landing requirement. Options considered included flaps attached to the outer diameter of the inflatable structure (see Figure 8a), flaps deployed on mechanical booms from the rigid center body (Figure 8b), and deforming quadrants of the HIAD structure by pulling inward on radial cables (i.e. reusing the retraction system). The estimated mass used in the mass model is based on four tabs with 6% of the HIAD area, with same areal mass as HIAD inflatable with TPS, plus inflation gas and actuators. This design is preliminary and the mass estimate that will be refined with future analysis. Over all, the aerocapture HIAD system had a mass of 3,778 kg and the EDL HIAD had a mass of 3,762 kg.

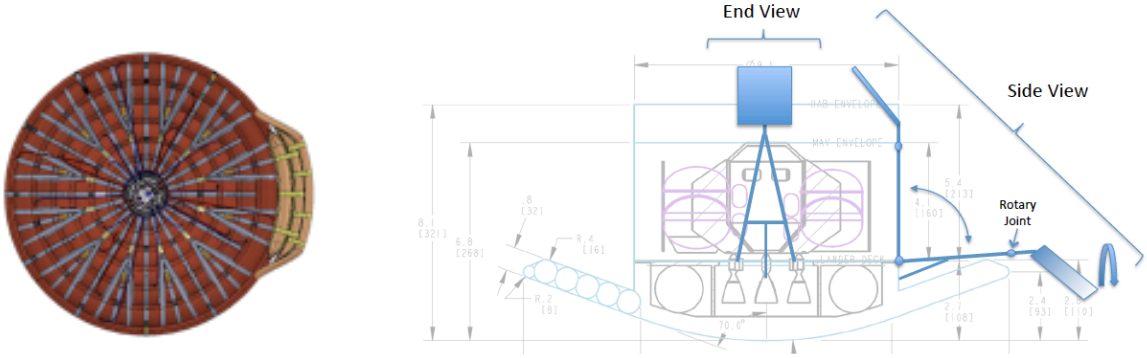

(a) **(b)**

Figure 8. Concepts for flap configurations on a HIAD aeroshell; (a) inflatable flap and (b) mechanically deployed flap.

		AC HIAD				EDL HIAD			
Rigid Structures	**Rigid Heatshield**	121	20%	24	145	330	20%	66	396
	Rigid Heatshield Door	0	20%	0	0	132	20%	26	158
	Gap Fillers*	0	20%	0	0	152	20%	30	182
	Attachment Ring Scar Mass	725	10%	73	798	639	10%	64	703
	Adapter Mass	725	10%	73	798	639	10%	64	703
	Sensor Package	50	10%	5	55	50	10%	5	55
Inflatable	**HIAD Inflatable Structure**	540	10%	54	594	376	10%	38	414
Inflation System	**HIAD Inflation System**	38	20%	8	46	45	20%	9	54
	HIAD Inflation Gas	5	25%	1	6	6	25%	2	8
Thermal Protection	**HIAD TPS**	754	10%	75	829	661	10%	66	727
Rails / Separation System	**Separation System Mass**	108	100%	108	216	14	100%	14	28
	HIAD Retraction System	N/A	N/A	N/A	N/A	150	33%	50	200
Tabs	**HIAD Trim Tab**	291	0%	0	291	316	0%	0	316
TOTAL		**3357**			**3778**	**3510**			**3762**

*Value not included in total mass

Images of the HIAD vehicle configuration in each mission phase are shown in Figure 9. While they are similar to ADEPT, key differences are noted. For example, in the *Launch* configuration, the inflatable structures are also stowed forward of the rigid heatshield, toward the lower portion of the SLS 10 m fairing as to not impact the packaging volume for the payload. Also, without the long ribs in the ADEPT design, the launch vehicle adaptor is shorter, so it uses less mass and provides a lower center of gravity in the launch vehicle fairing.

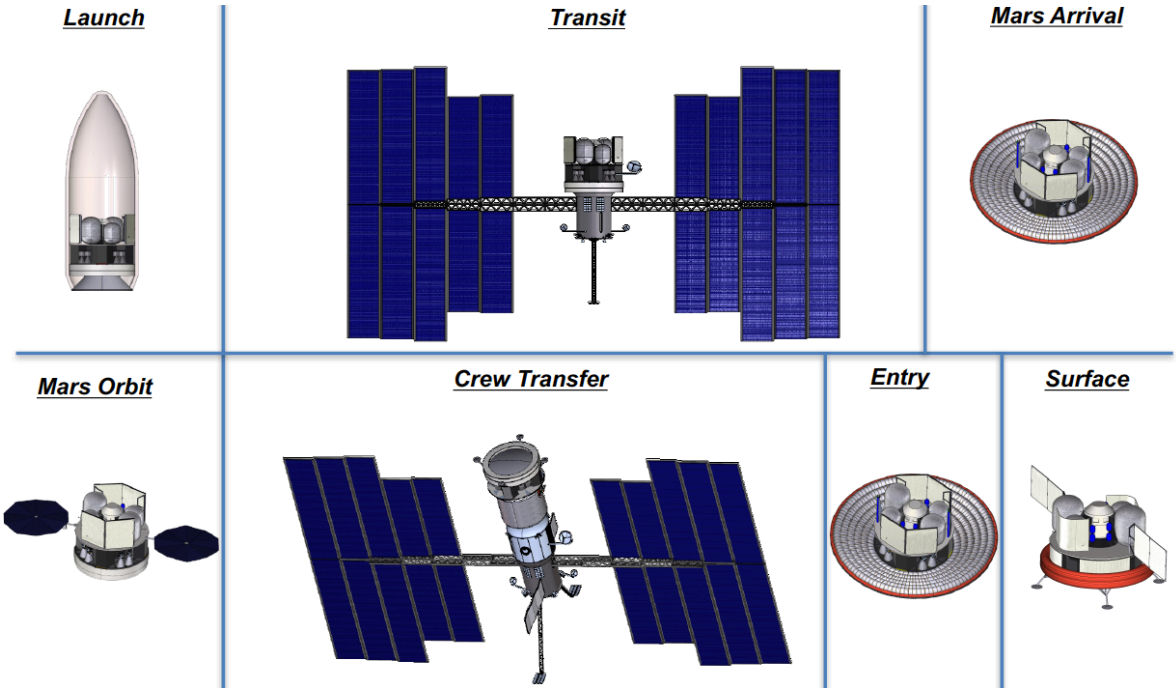

Figure 9. HIAD vehicle configurations for each phase of the mission.

After launch, the HIAD deployable structures remain in the stowed configuration throughout transit to Mars. The *Transit* configuration in Figure 9 shows the HIAD lander docked with the in-space transportation stage. The image depicts adequate clearance between the solar arrays of the transportation stage and the lander.

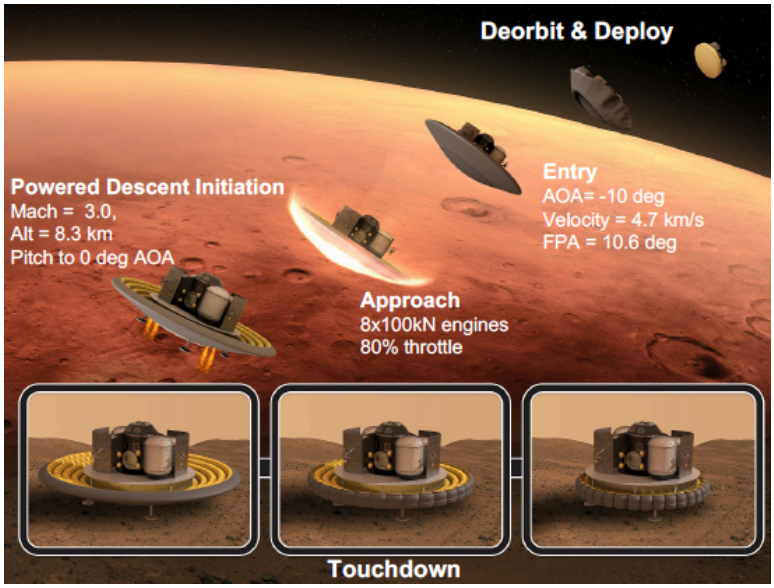

Figure 10. HIAD vehicle EDL concept of operations.

Once at Mars, the cargo mission performs aerocapture into a one Sol orbit (250 km x 33800 km). Therefore, two days prior to Mars arrival, the lander separates from the transportation stage. At that time the first HIAD is inflated and reorients for aerocapture. Unlike the ADEPT shape, the HIAD uses a symmetric aeroshell. Control flaps are not included in the *Mars Arrival* configuration image. After aerocapture, the inflatable and rigid heatshield are separated from the lander system.

Similar to the ADEPT lander design, the HIAD lander is powered by the transportation stage during transit. After separation and aerocapture, the lander must maintain power in orbit for up to one year. Therefore, the *Mars Orbit* configuration shows solar arrays deployed. For the lander that will deliver crew to the surface, it must dock with the crew transfer vehicle in a configuration that is opposite from the cargo lander transit (connected through the heat shield) so crew can enter directly into the habitat. The *Crew Transfer* image in Figure 9 shows that there is appropriate clearance from the transit stage assuming the orbiting arrays on the crew lander are stowed or jettisoned prior to docking.

Once the vehicle is ready to initiate the deorbit burn and perform EDL, the second HIAD is deployed and checked out. After the deorbit burn, the vehicle reorients to an EDL configuration using RCS thrusters. Details of the EDL vehicle configurations are shown in Figure 10. Again, no jettison events are allowed during EDL, so after peak heating and prior to engine initiation, doors open to expose the engines and landing gear. Once on the surface, the HIAD inflatable tori are deflated and retracted as shown in Figure 10 to simplify cargo offloading.

C. Master Equipment List

The master equipment list for each vehicle is summarized in Table 3. It is noted that the power, avionics and payload elements are identical between the vehicles. The propulsion mass is a function of the propellant used; more propellant means larger tanks and associated structures. Additional details of the subsystems are provided in Ref [14].

This section has summarized two deployable vehicle point designs, concepts of operations, and vehicle configurations to deliver 20 t payloads to the surface of Mars. The following section will describe the flight performance analysis and results that verify that both systems meet mission landing constraints.

Table 3. ADEPT and HIAD Master equipment list

ID	Subsystem	ADEPT	HIAD
1.0	Structures	5,422	5,422
2.0	Propulsion	4,963	4,916
3.0	Power	1,568	1,568
4.0	Avionics	333	333
5.0	Thermal	411	411
6.0	Aero decelerator	8,658	7,540
Dry Mass		**21,355**	**20,190**
7.0	Cargo	20,000	20,000
8.0	Non-Propelled Fluids	1,565	1,479
Inert Mass		**42,920**	**41,669**
9.0	Used Propellant	17515	15,564
Total Stage Gross Mass		**60,435**	**57,233**

III. Vehicle Performance

Similar low lift-to-drag (L/D) vehicles, with blunt forebody shapes, have flown guided entries at Mars using bank angle control and a L/D near 0.24, with a hypersonic phase angle of attack near 15 deg. For large human scale missions, earlier studies indicated that additional L/D, up to 0.3, would be needed to achieve landing accuracy desired for Mars missions using heritage bank angle guidance. However, the higher L/D results in angles of attack near 20 deg. Notional payloads being considered have heights of approximately 8 m above the lander deck. The combination of tall payloads and angles of attack near 20 deg guarantee flow impingement on the payload and require protection using a rigid backshell, thus eliminating the mass advantage of the deployable configurations. Therefore, new approaches for entry guidance are considered that allow the vehicle to maintain flight control to meet landing constraints with lower L/D (and lower angles of attack). The guidance approach is called direct force control (DFC) and assumes some mechanism is used to control aerodynamic forces independently. For example, flaps located at 90 deg intervals around the outermost deployed diameter can be modulated to control angle of attack and sideslip independently, or the aeroshell shape can be changed during flight using a tensioned cable system to deflect the deployed shape as is shown in Fig. 11. A movable mass device can be actuated to achieve the same effect. The DFC approach that reduces the required angle of attack and eliminates the risk of direct flow impingement on the payload; it also allows for more accurate targeting of the engine initiation condition, reduces the propellant use during descent, and enables landing within the desired 50 m from the target.

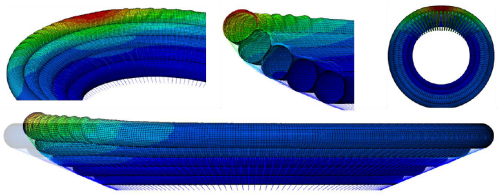

Figure 11. Example of a HIAD shape morphing.

This section presents the assumptions, analysis, and results of the flight performance to characterize the Low L/D human scale vehicle using different entry and descent guidance schemes. Initial EDLAS Phase 2 work presented the advantages of using DFC during entry [15]. As the vehicle designs matured, additional modifications were made to consider alternatives to descent guidance approaches. Due to the similar shape and mass estimates for the HIAD and ADEPT, this analysis assumes their flight performance is similar and so only one generalized vehicle is presented. The vehicle has a 16 m diameter with a 70 deg sphere cone forebody (deployable attached to a 9.1 m diameter rigid heatshield). The entry mass is 51t, the ballistic coefficient is 155 kg/m^2.

The Program to Optimize Simulated Trajectories II (POST2) is the trajectory simulation used to characterize performance for the guidance comparison. The simulation is initiated at deorbit of a polar one Sol orbit (250 km x 33800 km), therefore the entry velocity is 4.8 km/s. The entry time corresponds to a minimum in the Mars pressure cycle (May 10, 2033) and the landing target is near the equator. Three degree of freedom Monte Carlo analysis is performed using the HIAD aerodynamic model with uncertainties and the Mars Global Reference Atmosphere Model (Mars-GRAM 2010) [16]. The simulations assume perfect navigational knowledge and no dispersion of the entry state.

The analysis compares the vehicle performance of the low L/D vehicle using two different entry and powered descent guidance approaches. Results for both a bank angle and DFC entry guidance approach are presented. Bank angle rates, derived from the Apollo experience, are limited to a maximum of 20 deg/s and bank angle accelerations are limited to 5 deg/s^2. Bank reversals are performed using the RCS thrusters notionally located on the upper deck of the lander. In the absence of DFC experience for blunt body vehicles, angle rates and accelerations were selected with flight performance constraints and controller development in mind. Therefore, the maximum angle of attack rate and accelerations are set to 5 deg/s and 2 deg/s^2 respectively and the maximum sideslip angle rate and accelerations are 0.3 deg/s and 2 deg/s^2 respectively. As described in the EDL concept of operations in Figures 5 and 10, the vehicles ignite engines at approximately Mach 3. Therefore, to minimize propellant use and meet targeting constraints, the entry guidance seeks to minimize the dispersions at the engine initiation point. The analysis assumes that eight 100kN engines are modeled as a single engine with a specific impulse of 360 s. To provide margin for high fidelity simulations, the maximum throttle setting in the 3DOF trajectories is limited to 80%. Once the engines are on, two powered descent options are considered. The first is a pure gravity turn, in which the direction of thrust is aligned with the velocity vector, the descent guidance determines the pitch and yaw rates required to hold a zero-degree angle of attack and side slip. The second approach is called an augmented gravity turn. In this approach, the guidance algorithm determines the pitch and yaw rates to hold the desired angle of attack and sideslip angle that minimize landing errors. The primary difference in the approaches is the latter allows for small variations in the vehicle angle of attack and sideslip during decent where the former forces them to be zero degrees. The study assumes that all thrust variations are performed using differential throttling, not gimbaled engines. While the aerodynamic effect of trim tabs on blunt body rigid capsules has been characterized using wind tunnel tests [17], and ongoing studies explore movable mass

and morphing shape designs, the analysis herein seeks to characterize the performance needed from such a capability independent of implementation.

Parameters included in the Monte Carlo analysis are shown in Table 3. 8001 cases were run for three different scenarios: (1) bank angle guidance with pure gravity turn, denoted as BNKPGT, (2) bank angle guidance with augmented gravity turn (BNKAGT) and (3) direct force control with augmented gravity turn (DFCAGT). Key metrics include ability to meet the 50 m to target landing criteria, total propellent used, landed altitude and angle of attack at engine initiation. The results for each are shown in Figures 12 to 15.

Table 3. Monte Carlo parameters

Parameter	Dispersion /Distribution
Center of Gravity Location	±0.05 m 3σ
Mass	±500 kg 3σ
Aerodynamics Coefficients	MSL Aerodynamic Uncertainties
Atmosphere	Dust tau: 0.1-0.9 uniform Mars-GRAM 2010 density dispersions

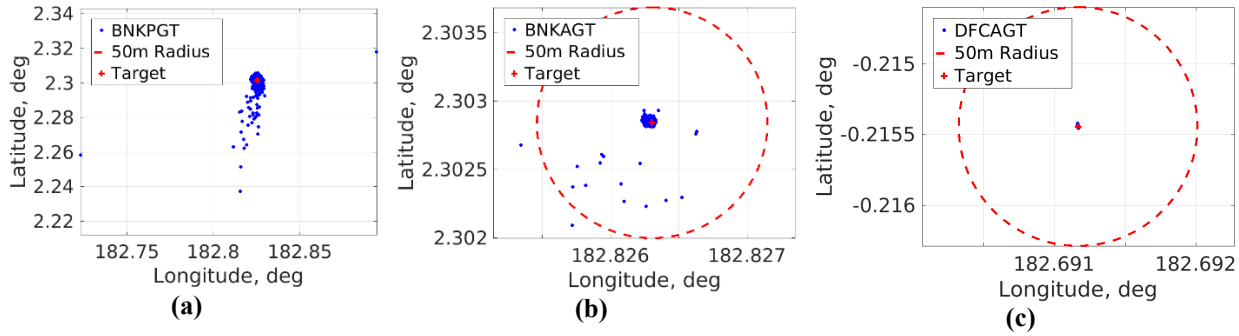

Figure 12. Monte Carlo landing foot print results.

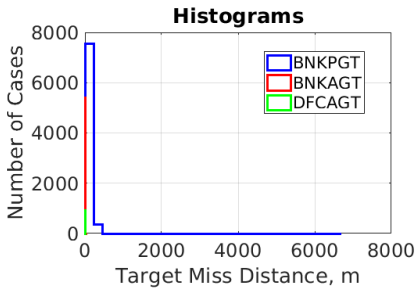

	BNKPGT	BNKAGT	DFCAGT
Mean	121.677	1.813	1.03
1-Sigma	146.804	1.653	0.208
2-Sigma	293.607	3.305	0.417
3-sigma	440.411	4.958	0.625
0.13 %-tile	4.603	0.262	0.111
1.00 %-tile	13.792	0.488	0.417
2.28 %-tile	19.681	0.662	0.542
50.00 %-tile	106.971	1.729	1.047
97.72 %-tile	267.839	2.866	1.397
99.00 %-tile	361.116	3.154	1.436
99.87 %-tile	1697.665	29.589	1.523
Max Value	6661.719	57.792	1.674
Min Value	2.265	0.16	0.003
Num Runs	8001	8001	8001

Figure 13. Miss distance (note scale).

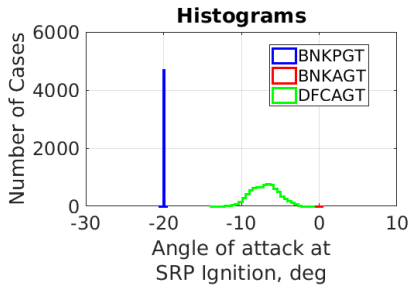

	BNKPGT	BNKAGT	DFCAGT
Mean	-20	0	-7.012
1-Sigma	0	0	1.801
2-Sigma	0	0	3.603
3-sigma	0	0	5.404
0.13 %-tile	-20	0	-12.718
1.00 %-tile	-20	0	-11.041
2.28 %-tile	-20	0	-10.436
50.00 %-tile	-20	0	-6.999
97.72 %-tile	-20	0	-3.434
99.00 %-tile	-20	0	-2.966
99.87 %-tile	-20	0	-2.237
Max Value	-20	0	-0.517
Min Value	-20	0	-13.887
Num Runs	8001	1	8001

Figure 14. Angle of attack at engine initiation.

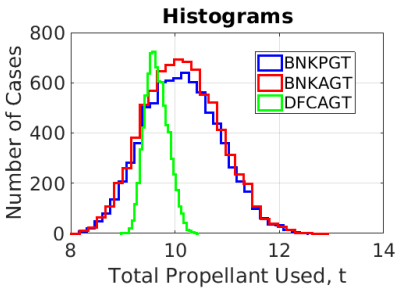

	BNKPGT	BNKAGT	DFCAGT
Mean	10.128	10.128	9.643
1-Sigma	0.715	0.716	0.218
2-Sigma	1.431	1.433	0.437
3-sigma	2.146	2.149	0.655
0.13 %-tile	8.311	8.308	9.128
1.00 %-tile	8.6	8.597	9.208
2.28 %-tile	8.788	8.786	9.255
50.00 %-tile	10.112	10.112	9.626
97.72 %-tile	11.578	11.576	10.101
99.00 %-tile	11.852	11.853	10.168
99.87 %-tile	12.221	12.222	10.316
Max Value	12.527	12.926	10.435
Min Value	8.086	8.086	8.982
Num Runs	8001	8001	8001

Figure 15. Total propellant used.

Figure 12 shows the landing points for the three different Monte Carlo scenarios. Figure 12a shows the effect of bank angle entry guidance and pure gravity turn. Many of the landing points miss the 50 m radius target by a mean of 122 m (See Figure 13 for values). However, the maximum miss distance is 6.6 km as shown in Figure 13. It is noted that other powered descent guidances may offer more fuel and targeting optimal landing solutions for bank angle guidance, but it does not solve the issue of flow impingement on the payload if the angle of attack remains near 20

deg as shown in Figure 14. The blue line in Fig 14 shows that the bank angle guidance, which flies with a constant 20 deg angle of attack through entry, has a 20 deg angle of attack at engine initiation. That attitude places additional burden on the descent system to reorient the vehicle for landing compared to the DFC entry guidance. Figure 12b shows the landing locations for the bank angle entry guidance and the augmented gravity turn. With the added control during the powered descent phase, the vehicle is able to clean up the landing dispersions errors seen in Figure 12a to nearly meet the landing criteria to land in the 50 m radius circle noted in the plot. However, the vehicle still flies at 20 deg angle of attack (under the blue line in Figure 13) and uses nearly the same amount of propellant with nearly the same dispersion, shown in Figure 15. However, when the DFC entry guidance is combined with the augmented gravity turn, all landing points land right at the target (within a couple meters) as seen in Figure 12c and miss distance statistics for DFCAGT shown in Figure 13. Therefore, not only does DFC reduce landing dispersions, it also reduces the angle of attack during entry and also at engine initiation shown by the green line in Figure 14. Additionally, DFC, with the augmented gravity turn, reduces the mean total propellant use by nearly 0.5t and reduced the maximum dispersion propellent by nearly 2t compared to the bank angle guidance cases. This significant result, along with the effective reduction of angle of attack during entry provided sufficient evidence to continue exploring the feasibility of developing a Direct Force Control guidance system for low L/D vehicles, one of the key recommendations from the study. Not shown are the statistics for landed altitude but all three scenarios meet the 0 km altitude criteria. While the reduced angle of attack does reduce the risk of direct convective flow impingement on the payload, there is still a risk of radiative heating on the payload that is addressed in the following section.

IV. Aft body heating

Flight mechanics results, presented in the previous section, demonstrated the ability of DFC to reduce the angle of attack during entry and reduce the risk of direct convective flow impingement on the payload. However, radiative heating will still impact the payload. This study considers the tallest payload configuration, the habitat, for the radiative heating analysis. An image of the payload configuration used in the analysis is shown in Figure 17. Over the course of the study the lander deck height as well as the lander grew as a result of the design updates. Figure 17a shows the vehicle configuration used for the aftbody heating study, and Figure 17b shows the updated packaged payload configuration. The change in payload height will affect the results and will be incorporated in to future efforts to characterize aftbody heating.

A one-dimensional thermal response model was developed to characterize the radiative heating on the aft body at five different locations on the vehicle (denoted by colored circles in Figure17a). The objective of the study is to identify the type and amount of insulation needed to protect the payload from radiative heating during entry. The results will determine whether localized thermal protection is adequate or if the vehicle requires a more massive rigid backshell-like structure. Therefore, this section summarizes the heating results and its impact on the payload.

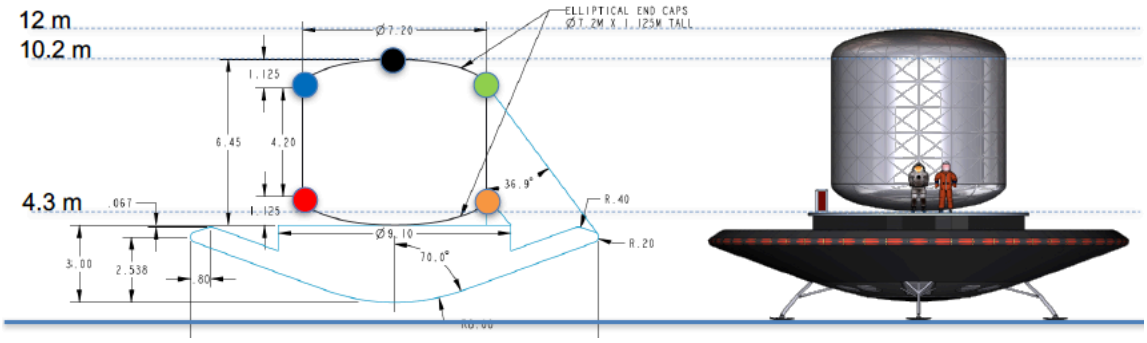

Figure 17. (a) Vehicle configuration used for the heating analysis; (b) Updated version of the vehicle design.

Each lander has different payload elements and different payload material requires different TPS solutions. For example, the original outer material of the lander deck is bare aluminum and the habitat outer material is black Kapton. The Mars Ascent Vehicle has large propellant tanks with outer material made of aluminized Teflon and T300 composite radiators covered with ultra-low solar absorbance paint. Table 4 contains several key payload components, defines layered materials and temperature limits for reference.

The heating analysis uses the nominal trajectory conditions corresponding to the DFCAGT trajectory described in the previous section. The nominal trajectory has a maximum entry angle of attack of -6 deg. The color dots denote the

location of the analysis and correspond to the colors depicted on plots showing the unmargined heating results in Figure 18. The complete description of the heating analysis is reported in Ref [18].

Table 4. Payload layer materials and temperature limits.

Component	Outer surface with AZW/LA-II low-α paint outer coating	Under outer surface	Temperature limits
MAV MPS tanks	0.075" Al Vacuum Jacket	High-temp MLI (Double Aluminized Kapton) 60 layers	MLI: 400C (673K) intermittent, 290C (563K) continuous
Radiator panels	0.039" T300 composite panel		800K
Crew cabin	Proposed 0.060" Al substrate for low-α paint	High-temp MLI (Double Aluminized Kapton) 60 layers	MLI: 400C (673K) intermittent, 290C (563K) continuous
Lander deck	Avg 9.0 kg/m^2 Al 2219-T851 skin panel with stiffening webs		543C (816K)

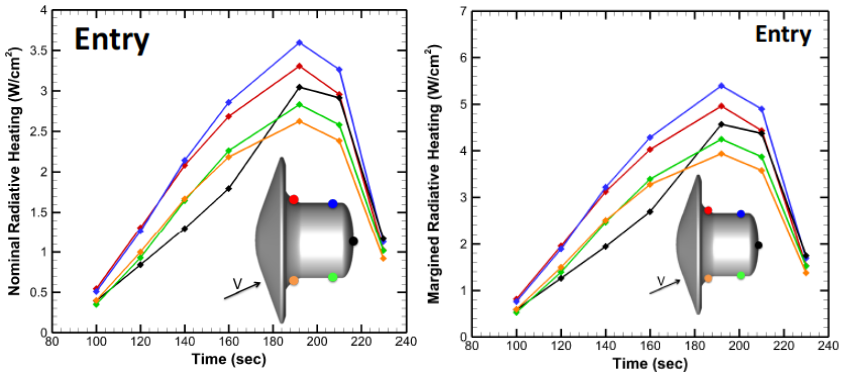

(a) (b)

Figure 18. a) Unmargined radiative heating results on the aftbody; b) margined radiative heating.

Figure 18a shows the unmargined rediative heating, which is highest near the top of the payload on the side opposite of the oncoming flow. The margin on the radiative heating is 50%. The total margined radiative heating is shown in Figure 18b.

Based on this heating analysis, a COMSOL [19] one dimentional themal response model was developed that used the time dependent heat pulse with a maximum of 350 J/cm^2. The model also included the incoming radiative flux absorbed by the surface and radiative surface cooling, given optical properties of the outer material exposed to the flow. Solar radiation is ignored because it is negligable compared to the incoming shock-layer radiation. Given these environments, the required protection using aluminized Kapton over the outer materials of each aftbody payload component was assessed to stay within temperature limits. The initial temperature of the outer surface is assumed to be 261 K. The analysis also assumes that the habitat and lander deck interface has been smoothed to simplify calculations.

The radiative thermal model is represented in the Figure 19 where the q_{net} term represents net heat flux at the outer material surface, α is the absorptivity of the outer layer material, q_R represents heat flux due to shock-layer radiation, computed from LAURA/HARA [20] and q_{RS} is the heat flux due to heat rejection from a radiating surface.

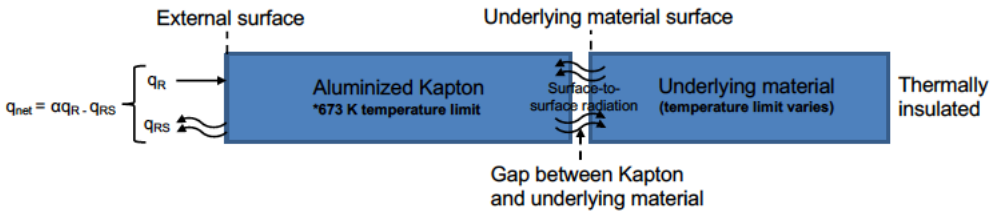

Figure 19. Thermal model diagram

The absorptivity for each material varies as a function of incident wavelength and wavelength varies with temperature. Therefore, the absorptivity of spacecraft materials is generally measured compared to solar flux. Because the incoming radiation from the shock layer is from the infrared spectrum, infrared absorption offers a more realistic case rather than using the reported solar absorptance. The absorptivity will be different at infrared wavelengths compared to absorptivity at solar wavelengths. Until recently, no data for absorptivity at infrared wavelengths was available. Therefore, for conservatism, absorptivity was assumed equal to the reported infrared emittance rather than using solar absorptivity value.

The initial results of the study indicated that no additional thermal protection is needed for a bare aluminum lander deck, and the peak temperature can vary from 285-338 K, depending on the thickness of the deck. The habitat requires the thickest amount of aluminized Kapton at 0.3 mm to protect black Kapton material. This thickness would require approximately 73 kg of aluminized Kapton to protect the entire current habitat design. However, if the black Kapton on the habitat was removed and only bare aluminum was used, no additional thermal protection would be needed. As for the other payload elements considered, the Mars Ascent Vehicle radiator panels and tanks need 0.21 mm of Al Kapton. The required Al Kapton thickness is driven by Kapton temperature limit and the fact that Kapton melts if it is thinner. However, radiators do not operate efficiently when covered with insulation. This study did not address the complication of removing insulation from the radiators so alternate solutions are being considered.

Initial analysis shows that light-weight TPS material can mitigate radiative heating; no additional TPS is needed on the lander base, composites coated with ultra-low solar absorptivity paint would be sufficient, and other elements need only thin layers of aluminized Kapton to protect from radiative heating. These approaches to mitigate radiative heating, in addition to flying the vehicle at lower angles of attack, support the decision to eliminate the rigid backshells for the deployable vehicles. However, large margins on convective heating, up to 200% based on the Mars Science Laboratory experience [21], have not yet been considered. If the margins cannot be reduced through flight data from Mars 2020 and Orion missions, which have thermal sensors on the backshell, then additional insulation will be required to mitigate convective heating. The TPS mass and impact to individual payload element to mitigate convective heating has not yet been analyzed. Therefore, no definitive decision has been made as to whether a rigid backshell is needed to protect the payloads of the deployable vehicles.

V. Recommendations

Low L/D, low ballistic number configurations (ADEPT and HIAD) have similar forebody shape and ballistic coefficient. However, ADEPT deployable technology is at lower technology readiness level (TRL). Additional testing is needed to validate the flight stability of large areas of unsupported fabric between ribs. The proposed TPS is over qualified for Mars aerocapture and entry conditions considered in this study. The ablator TPS could be replaced with a lighter weight, flexible TPS material but it also has not been shown to support loads stretched between ribs. Including additional ribs to reduce the unsupported area adds mass to the system. The deployment and retraction system are at low fidelity and risk increasing mass and reducing the payload volume. Surface retraction risks interfering with payload offloading. Additional work is also needed to evaluate and demonstrate folding/unfolding, and large-scale manufacturability for the ADEPT concept.

Much of the analysis that remains for other Low L/D configurations, in guidance and control and CFD analysis to understand the vehicle in the supersonic flow environment, are similar for HIAD and ADEPT. The ADEPT design is at a lower TRL. It is for these reasons we recommend continuing study using only the HIAD low L/D vehicle in order to focus future investments and the analysis in areas that are common to both concepts. For example, since direct force control has shown that it is important to achieve the required performance in the trajectory simulations for all low L/D vehicles considered, it is recommended that future studies identify feasible implementations of DFC for the low L/D vehicle configuration. Second, analysis indicates that the low L/D vehicles must initiate engines in supersonic flow. There is limited flight data in the regimes and under the conditions assumed for these engines. Also, the flight performance and vehicle controllability are highly dependent on accurate characterization of the supersonic retropropulsion during descent. Therefore, it is recommended to perform extensive CFD analysis of the supersonic

retro-propulsion (SRP) initiation phase to characterize vehicle controllability and the SRP aerodynamic force interactions.

VI. Conclusion

This paper describes the work of the EDLAS Phase 2 study that has refined the concept of operations and point designs for two deployable vehicle concepts to deliver 20t payloads to the surface of Mars. The primary advantage of the deployable systems is the light weight material, compared to a rigid aeroshell, that also enable drag areas beyond the launch fairing diameter limits. Likewise, the vehicles rely on the deployable diameter to protect the payload. Analysis presented herein has shown that, based on the assumption of using an augmented gravity turn guidance for powered descent, that direct force control (DFC) guidance does offer many advantages to reduce entry angle of attack, reduce propellant use and improve landing targeting. Therefore, a study recommendation is to continue technology investments in characterizing feasible implementation methods for DFC. The analysis and data presented herein to mitigate aft body heating depends on the details of each individual payload element. While only notational payloads are considered here, additional heating analysis is needed as the design and packaging configurations mature.

In conclusion, NASA has established a multi-directorate, multi-center, multi-year collaboration to identify technologies to enable human scale EDL at Mars. Every assumption in the Mars architecture has significant design implications that impact vehicle design from pre-Earth launch to Mars ascent. Establishing payload definitions provided depth of analysis not afforded human scale EDL design in past studies. And while the vehicles that fly will likely not look like the vehicles designed in the study, fundamental understanding gained by effort is driving near and far term technology investments.

Acknowledgments

The authors would like to acknowledge the Science Technology Mission Directorate (STMD) and the Human Exploration and Operations Mission Directorate (HEOMD) for their continued support of this and other studies that continue to challenge our EDL paradigms. The authors would like to recognize specific individuals who made significant contributions to the work presented herein including Mike Baysinger, Chad Brivkalns, R. J. Bodkin, Neil Cheatwood, Tim Collins, John DiNonno, Joseph Garcia, Steve Hughes, Chris Johnson, Dave Paddock, Richard Powell, Jamshid Samareh, Steve Sutherlin, John Teter, H. Dan Thomas, Bryan Yount and all the members of the EDLAS Team. They come from many NASA centers including, Ames Research Center, Langley Research Center, Johnson Spaceflight Center and Marshal Space Flight Center, as well as, external contractors and those in academia. While they are too numerous to list here, the work summarized in this paper is based on their collective contributions.

References

[1] Cianciolo, A. D. and Polsgrove, T. T., "Human Mars Entry, Descent and Landing Architecture Study Overview," AIAA Paper 2016-5494, Sept. 2016.

[2] Cassell, A. M., Brivkalns, C. A., Bowles, J. V., Garcia, J. A., Kinney, D. J., Wercinski, P. F., Cianciolo, A. D. and Polsgrove, T. T. "Human Mars Mission Design Study Utilizing the Adaptive Deployable Entry and Placement Technology" 2017 IEEE Aerospace Conference, 4-11 March 2017.

[3] Polsgrove,T. T., Thomas, H. D., Cianciolo, A. D., Collins, T., Samareh, J. "Mission and Design Sensitivities for Human Mars Landers Using Hypersonic Inflatable Aerodynamic Decelerators" 2017 IEEE Aerospace Conference, 4-11 March 2017.

[4] Polsgrove, T. T., Percy, T. K., Garcia, J., Cianciolo, A. D. Samareh, J., Lugo, R., Robertson, E., Cerimele, C., Sostaric, R., and Garcia, J., "Human Mars Entry, Descent and Landing Architecture Study: Rigid Decelerators," AIAA SPACE 2018 Abstract Submitted. Sept. 2018.

[5] Cianciolo, A. D. and Polsgrove, T. T., "Human Mars Entry, Descent and Landing Architecture Study: Phase 2 Summary," AIAA SPACE 2018 Abstract Submitted. Sept. 2018.

[6] Jefferies, S., Collins, T., Cianciolo, A. D., Polsgrove T. "Impacts of Launch Vehicle Faring Size on Human Exploration Architectures" 2017 IEEE Aerospace Conference, 4-11 March 2017 10.1109/AERO.2017.7943833

[7] Strauss, E. L., "Super Ablative Systems for Mars Lander Thermal Protection," Journal of Spacecraft and Rockets, Vol. 4, No. 10, Oct. 1967, pp. 1304–1309.

[8] Calculix Reference: http://www.calculix.de/

[9] Yount, Bryan, C., et al. "Structures and Mechanisms Design Concepts for Adaptive Deployable Entry Placement Technology" AIAA Aerodynamic Decelerator Systems Technology Conference, March 25-28, 2013, Daytona Beach, FL.

[10] Drake, B. (editor), "Human Exploration of Mars Design Reference Architecture 5.0," NASA/SP-2009-566.

[11] Dwyer Cianciolo, A.M., et al., "Entry, Descent and Landing Systems Analysis Study: Phase 1 Report," NASA–TM–2010–216720, July 2010.

[12] Dwyer Cianciolo, A.M., et al., "Entry, Descent and Landing Systems Analysis Study: Phase 2 Report on Exploration Feed-Forward Systems," NASA/TM–2011–217055, February 2011.

[13] Olds, A. D., Beck, R., Bose, D., White, J., Edquist, E., Hollis, B., Lindell, M., and Cheatwood, F. N., "IRVE-3 Post Flight Reconstruction." AIAA-2013-3398.
[14]Percy, T. K. et al. "Human Mars Entry, Descent and Landing Architecture Study: Descent," AIAA SPACE 2018 Abstract Submitted. Sept. 2018.
[15] Cianciolo, A. D., and Powell, R. W. "Entry, Descent and Landing Guidance and Control Approaches to Satisfy Mars Human Mission Landing Criteria", AAS Paper 17-254, February 2017.
[16] Justus, C. G., Johnson, D. L., "Mars Global Reference Atmospheric Model 2001 Version (Mars-GRAM 2001): Users Guide" NASA/TM-2001-210961.
[17]Horvath, T. J., O'Connell, T. F., Cheatwood, F. M., Prabhu, R. K., Alter, S. J., "Experimental Hypersonic Aerodynamic Characteristics of Mars Surveyor 2001 Precision Lander with Flap," *Journal of Spacecraft and Rockets*, Vol. 43, No. 2, March-April 2006, pp. 270-281.
[18] West, T. K., Theisinger, J., Brune, A. J., and Johnston, C. O. "Backshell Radiative Heating on Human-Scale Mars Entry Vehicles", AIAA Paper 2017-4532, June 2017.
[19] COMSOL, Comsol multiphysics user's guide, v5.0, Tech. rep., COMSOL/CM-010004.
[20] Mazaheri, A., Gno_o, P. A., Johnston, C. O., Kleb, B. "Laura User's Manual" 5.5-65135, Tech. rep., NASA/TM-2011-217800 (Feb. 2012).
[21] Edquist, K. T., Dyakonov, A. A., Wright, M. J., Tang, C. Y., "Aerothermodynamic Environments Definition for the Mars Science Laboratory Entry Capsule," AIAA Paper 2007-1206, 45th AIAA Aerospace Sciences Meeting and Exhibit, Reno, NV, 2007. doi:10.2514/6.2007-1206.